RSC Advances

PAPER

View Article Online
View Journal | View Issue

Cite this: *RSC Adv.*, 2020, **10**, 23491

Radical-dominated reaction of CO–NO on a $CaFe_2O_4$ surface in sintering flue gas recirculation†

Chaoqun Li, [ac] Qingzhen Han,[a] Tingyu Zhu[ab] and Wenqing Xu *[ab]

The catalytic reduction behaviours between NO and CO on a $CaFe_2O_4$ surface were studied using flue gas recirculation. The reaction mechanism and control principle were investigated *via* experiment and theoretical calculations. The experiment results show that $CaFe_2O_4$ can catalyse the reduction of NO by CO, and the NO conversion rate increases with the increase in CO concentration. The theoretical calculations indicate that the CO–NO reaction on $CaFe_2O_4$ surfaces complies with the Eley–Rideal mechanism, and the reaction path is controlled by nitrogen, oxygen and isocyanate radicals. Specifically, the dissociation of NO into nitrogen and oxygen radicals, and the formation of subsequent isocyanate radicals dominate the reaction. The results provide new insight into the intrinsic reaction mechanism and the meso-scale control principle, allowing us to propose a novel process design scheme to improve the NO_x emission reduction efficiency in the flue gas recirculation process.

Received 3rd January 2020
Accepted 9th June 2020

DOI: 10.1039/d0ra00064g

rsc.li/rsc-advances

1. Introduction

The reduction of NO_x emission has gained much attention owing to its role in the formation of photochemical smog and acid rain.[1] The iron ore sintering process can discharge approximately 0.1 million tons of NO_x annually, accounting for approximately 48% of the total emissions from the iron and steel industries.[2,3] A lot of studies have been done in order to decrease NO_x emission, but as the emission control regulations get stricter, NO_x reduction remains a challenging problem.

There are two methods used to inexpensively reduce NO_x emissions from sintering plants. One method is the treatment of exhaust gas.[4–7] However, the large exhaust emission (around 100 m^3 (m^2 $min)^{-1}$) and low NO_x emission concentration (200–300 ppm)[2,3] lead to huge capital investment and high operational cost, which makes it difficult to apply this method and have reduced the competitiveness of the plants. Another method is to reduce NO_x through combustion control during the sintering process.[8–12] The flue gas recirculation technique was proposed on this basis, and it is beneficial to the reduction of flue gas volume.[13–15]

Fig. 1 shows the typical flow process of the flue gas recirculation technology, selecting specific flue gas in the bellows and sending it back into the circulation hood for re-combustion.[10,15] A recent study reported that when the proportion of flue gas recirculation is 30%, the NO_x emission reduction can reach 15.51% at most.[16]

The reduction of NO_x *via* flue gas recirculation is mainly due to the changes in the combustion atmosphere and the occurrence of NO_x reduction reactions.[17] Compared with conventional sintering process, flue gas recirculation sintering process has a low oxygen content, and a large amount of pollutants enter the combustion bed.[18] Take the process design in Fig. 1 as an example, the oxygen content of circulating flue gas is about 16%, CO ~ 1% and NO ~ 400 ppm. Firstly, fuel combustion leads to a continuous decrease in the oxygen content, which is conducive to the conversion of fuel N to nitrogen,[17] and reduces the generation of NO_x.[18] Secondly, the NO_x generated and carried can be reduced on the surface of coke.[19] In addition, calcium ferrite, main products of iron ore sintering,[20,21] has been proven that there is a good catalytic effect on the reduction of NO by CO in local anaerobic conditions.[22–25] Compared with

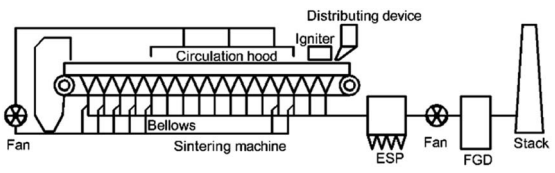

Fig. 1 Schematic diagram of the flue gas recirculation technology.

[a]*Research Center of Process Pollution Control, National Engineering Laboratory for Hydrometallurgical Cleaner Production Technology, State Key Laboratory of Multiphase Complex Systems, Institute of Process Engineering, Chinese Academy of Sciences, No. 1, 2nd North Lane, ZhongGuanCun, Beijing 100190, China. E-mail: wqxu@ipe.ac.cn*

[b]*Center for Excellence in Regional Atmospheric Environment, Institute of Urban Environment, Chinese Academy of Sciences, Xiamen 361021, China*

[c]*University of Chinese Academy of Sciences, Beijing 100049, China*

† Electronic supplementary information (ESI) available. See DOI: 10.1039/d0ra00064g

other combustion processes, the special high temperature anaerobic atmosphere and the catalysis of the products make this reaction attract wide attention in the study of NO reduction in sintering.[26,27]

Although many researches of the CO–NO reaction in flue gas recirculation have been done,[12,18,27–29] the intrinsic reaction mechanism and the control principle with the microscopic electronic structures are still not quite clear. Metallurgists had hypothesized that the catalytic process consists of two steps: iron-bearing minerals are reduced to lower valence oxides by CO, and then NO is reduced to N_2 by lower valence oxides.[11,16] Unfortunately, due to the small specific surface area of the material and the high reaction temperature, it is difficult to obtain direct experimental evidence to support the hypothesis.

Therefore, a further systematic research of the CO–NO reaction on $CaFe_2O_4$ surface is required. In this manuscript, aiming at uncovering the intrinsic reaction mechanism, the CO–NO reaction on $CaFe_2O_4$ surface will be studied through experimental design and DFT calculation. The results were conducive to further understanding of the NO_x eliminate mechanism and the meso-scale control principle during flue gas recirculation sintering.

2. Materials and methods

2.1 Synthetic procedures

The $CaFe_2O_4$ in this work was synthesized by solid sintering methods using ferric oxide (Fe_2O_3) and calcium carbonate ($CaCO_3$) as precursors. $CaFe_2O_4$ were prepared by following steps. The precursors were first mixed in a mortar at a molecular ratio of 1 : 1. After mixing, the powder was then tableted and placed into a muffle furnace to be calcined for 12 hours in air at 1150 °C.

2.2 Experimental setup and activity test

The activity tests were evaluated in a continuous-flow fixed-bed quartz microreactor (Fig. S1,† i.d. = 4 mm) from 200 °C to 600 °C with 3 g of sample (40–60 mesh). The reaction was kept at 5 min for temperature improvement and 55 min at each temperature to ensure steady state operation. The default gaseous hourly space velocity (GHSV) is approximately 95 000 h^{-1}, which is designed to eliminate the effects of external diffusion in order to study the intrinsic reaction. The reaction conditions are feeding 0–1% CO, and 0–500 ppm NO, with Ar balance. The inlet and outlet gases were monitored using a FTIR spectrometer (Nicolet 6700) equipped with a 2 m gas cell and a DTGS detector with a resolution of 0.5 cm^{-1}. The collection region was 4000–600 cm^{-1} and 16 scans per time.

2.3 Material characterization

The X-ray powder diffraction (XRD) patterns of the various specimens were collected by an X-ray powder diffractometer (Bruker D8 ADVANCE Diffractometer) with Cu Kα radiation (λ = 0.15406 nm) operated at 40 kV and 40 mA. The patterns were measured over a 2θ range of 5–80° with a scanning step of 0.02°.

Diffuse reflectance infrared Fourier transform spectroscopy (DRIFTS) were obtained using a Nicolet 6700-FTIR equipped with a smart collector and a liquid N_2 cooled MCT detector. The flow of the feed gas mixture was controlled by MFCs. Prior to each experiment, the sample (approximately 30 mg) was pre-treated with pure Ar at 500 °C for 1 h, and then cooled to room temperature (25 °C). All spectra were obtained with a resolution of 4 cm^{-1} and accumulating 32 scans. A background spectrum was subtracted from each spectrum.

2.4 Theoretical methods

All calculations presented in this work were performed with the Cambridge Serial Total Energy Package in the Materials Studio package[30] based on the plane-wave ultrasoft pseudo potential method of the density functional theory (DFT). The exchange–correlation potential was described by the Perdew–Burke–Ernzerhof (PBE) functional of the generalized gradient approximation (GGA).[31] The cut off energy for the plane-wave basis set was set at 380 eV. The Monkhorst–Pack scheme *k*-point grid sampling for the Brillouin zone was set as 3 × 3 × 3 for the $CaFe_2O_4$ unit cell, and 3 × 3 × 1 for the $CaFe_2O_4$ surface models. The convergence criterion for the self-consistent field (SCF) was set at 5.0×10^{-7} eV per atom. All the atom coordinates are fully optimized until the forces on every atom were smaller than 0.01 eV $Å^{-1}$. The interaction between the valence electrons and the ionic core was described by the ultrasoft pseudo potential.

Finally, the band structure, the electronic densities of states, and the electron localization function of the optimized $CaFe_2O_4$ unit cell were calculated by GGA for the exchange–correlation functional information.

The adsorption energy E_a is defined by the following formula:

$$E_a = E_{total} - E_c - E_g, \quad (1)$$

where E_c is the energy of an isolated catalyst surface, and E_{total} is the total energy of the catalyst surface and the adsorption reactant gases. The energy of reaction gases NO, CO, CO_2, and N_2 is denoted by E_g. All the simulations of the elementary reactions with different reaction paths were carried out at 298.15 K and 1 atm.

3. Results and discussion

3.1 Activity

The NO conversion over $CaFe_2O_4$ and SiO_2 was conducted under the conditions of 400 ppm NO, 1% CO and Ar balance at a GHSV of 95 000 h^{-1} within 200–600 °C. As shown in Fig. 2, CO can react with NO under SiO_2 filling when the temperature is higher than 350 °C, but the maximum conversion rate of NO is only 10% at 600 °C under the experimental conditions. When filling $CaFe_2O_4$, the reaction can occur at 300 °C, and 100% NO conversion was obtained at 500 °C. In addition, NO_2 and N_2O were not detected in the whole reaction process (Fig. S2†).

SiO_2 is inert, so it can be considered that when SiO_2 is filled, the homogeneous reaction occurs between the gas CO and NO,

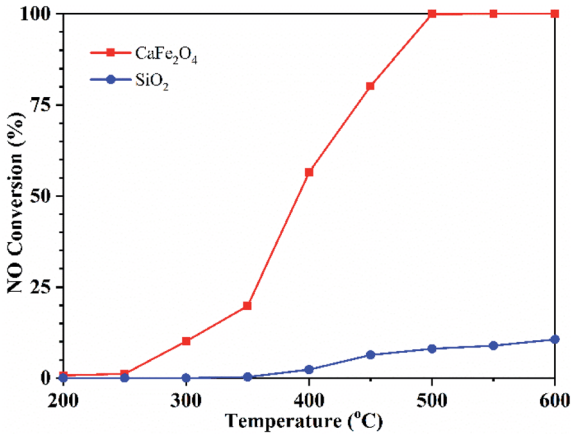

Fig. 2 NO conversion over $CaFe_2O_4$ and SiO_2 at different temperatures. Reaction conditions: 1% CO, 400 ppm NO, Ar balance, GHSV 95 000 h^{-1}.

and the NO conversion is very low when the reaction is below 600 °C. The filling of $CaFe_2O_4$ significantly improved the NO conversion at low temperature, which reduced the reaction activation energy. These results indicate that $CaFe_2O_4$ can catalyse CO to reduce NO during sintering flue gas recirculation.

3.2 Mechanism

To determine how the reaction occurred, the adsorption of CO and NO was confirmed by *in situ* DRIFTS adsorption experiments, and the dynamic DRIFTS spectra with time are given in Fig. 3.

As shown in Fig. 3(a), when the $CaFe_2O_4$ was exposed to a flow of CO, bands appeared at 2220–2050 cm^{-1}. This was ascribed to the gaseous CO molecular vibration peak. Besides, CO adsorption peaks were not observed on the graph, so it can be inferred that CO does not adsorb on the $CaFe_2O_4$ surface.

The $CaFe_2O_4$ was exposed to a flow of NO, and the corresponding changes are displayed as a function of time in Fig. 3(b). As can be seen, the bands at 1627 cm^{-1}, 1600 cm^{-1}, 1489 cm^{-1}, and 1340 cm^{-1} appeared. According to previous studies, we ascribed the bands at 1627 cm^{-1} to bridging bidentate nitrate, and at 1600 cm^{-1} to chelated double ligand nitrate.[32] The bands near 1489 cm^{-1} were related to monodentate nitrate[33] and the peaks at 1340 cm^{-1} were associated with the nitrocompound.[11,34] As the adsorption time increases, chelated double ligand nitrate and bridging nitrates first appear, followed by monodentate nitrates and nitrocompound, indicating that NO can continue to adsorb on the catalyst surface. Based on the gas adsorption results observed in *in situ* DRIFTS, it could be inferred that CO may participate in the reaction in a gaseous state, that is, the reaction may accord with the Eley–Rideal reaction mechanism.

3.3 Calculation results

According to the XRD crystal data (Fig. S1†), the calculation model of the $CaFe_2O_4$ crystal structure is constructed and optimized (Fig. S3†). The results showed that the $CaFe_2O_4$ shows a distinct spinel structure, and belongs to the primitive-cantered structure with a space group of *Pnma*. The optimized lattice parameters *a*, *b*, *c*, and space group (Table S1†) are in good agreement with the former experimental measurements from XRD data in this work and the literature.[35]

In order to explore the activity and the active centres of the NO–CO catalytic reaction, the band structure, the electronic density of states, and the electron localization function of the $CaFe_2O_4$ are analysed. Fig. 4(a) depicts the band structure of the optimized $CaFe_2O_4$ unit cell. The Fermi surface is close to the energy level (−0.278 eV → 0.0 eV) above the valence band top, which demonstrates that $CaFe_2O_4$ is a p-type semiconductor, and there are more free holes in the valence band that can accept electrons from reactions and activate the nearby atoms on the $CaFe_2O_4$ surface. The Fe partial density of states in $CaFe_2O_4$ (Fig. 4(b)) indicates that this energy level (−0.278 eV → 0.0 eV) is mainly composed of the d orbital of Fe atoms, showing that the Fe atoms and the nearby atoms possess high catalytic activity for reduction reactions. The electron localization

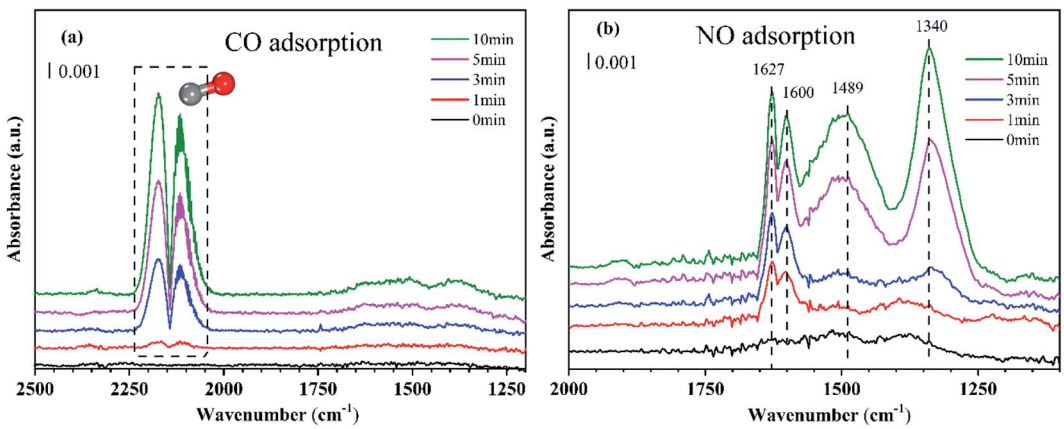

Fig. 3 Dynamic changes of *in situ* DRIFTS for the $CaFe_2O_4$ as a function of time in a flow of (a) CO and (b) NO at 50 °C. Reaction conditions: (a) 1% CO, Ar balance; (b) 400 ppm NO, Ar balance.

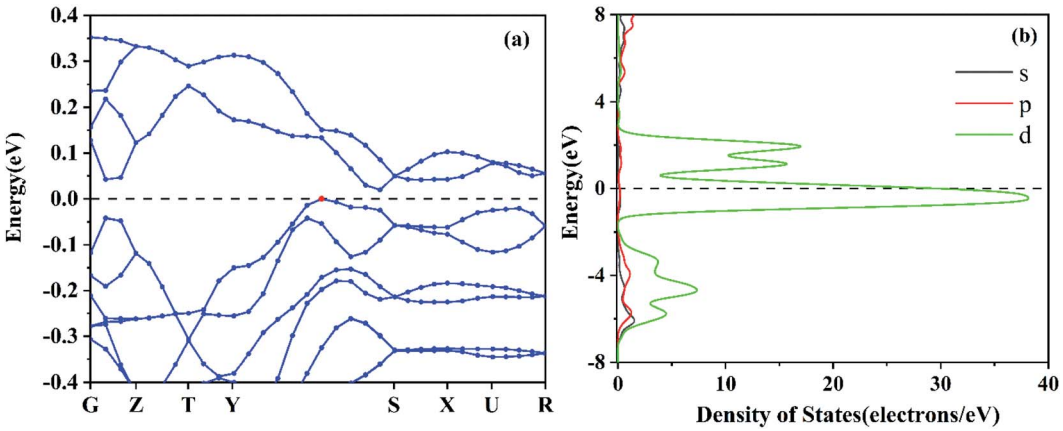

Fig. 4 Band structure (a) and Fe partial density of states (b) of the optimized $CaFe_2O_4$ unit cell.

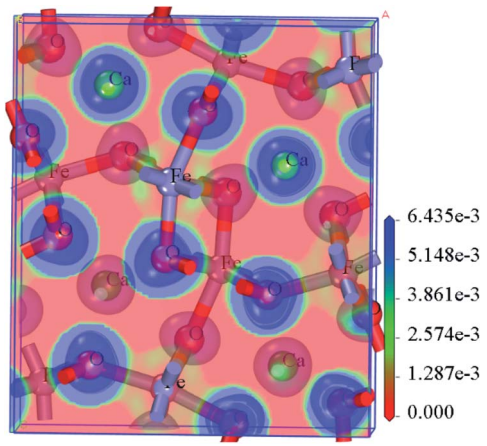

Fig. 5 Electron localization function of the optimized $CaFe_2O_4$ unit cell.

function (Fig. 5) also demonstrates that there is weak interaction between some Fe atoms and the surrounding atoms, which indicates that these Fe atoms and their nearby O atoms may be the active centres of the catalytic reaction.

To select the suitable crystal surface, all the $CaFe_2O_4$ surfaces were built and optimized based on the optimized structure of the $CaFe_2O_4$ unit cell. The $CaFe_2O_4$ crystal surfaces work functions of (110), (001), (100), (111), and (101) are 4.271 eV, 4.547 eV, 5.241 eV, 4.602 eV and 5.011 eV, respectively. Obviously, the $CaFe_2O_4$ (110) surface work function is the smallest, indicating that the catalytic activity of the $CaFe_2O_4$ (110) surface is the highest. So, the $CaFe_2O_4$ (110) was selected as the catalytic reaction surface. Then the 10-layer-atoms periodic structure of $CaFe_2O_4$ (110) adsorbed the NO and CO molecules (Fig. S5†) was adopted as the best adsorption method. The initial adsorption distance was set at 2.5 Å. For each gas molecule, the steadiest adsorption structure with the lowest energy was determined by comparing lots of optimized structures from different initial configurations designed by *in situ* DRIFTS.

Furthermore, the adsorption methods for all reactants (NO and CO) and products (CO_2 and N_2) were optimized and analysed on $CaFe_2O_4$ (110). The adsorption energies E_a (Table S2†) of reaction gases CO, NO, CO_2, and N_2 on the $CaFe_2O_4$ (110) surface are −0.57 eV, −2.54 eV, −9.48 eV and −1.84 eV, respectively, which illustrates that the adsorption rate-control step is CO adsorption, and the desorption rate-control step is CO_2 desorption. In addition, the work function (Table S2†) of the catalytic reaction system after NO adsorption and CO adsorption are 4.727 eV and 4.831 eV, respectively, showing that the surface electrons of the catalyst are easier to excite after NO adsorption, and the reaction occurs more easily. It is clear that NO gas molecules are first activated and dissociated on the $CaFe_2O_4$ (110) surface.

Fig. 6 intuitively shows the electron interactions between NO, CO, and the surface of the catalyst. It shows that after NO adsorption on the $CaFe_2O_4$ (110) surface, the NO electrons transfer to the Fe atoms (0.55e → 0.91e) and nearby O atoms (−0.67e → −0.71e), resulting in an increase in catalytic activity. Moreover, the N–O interaction in the NO molecule is weakened, leading to NO dissociation by activation. The NO and CO partial

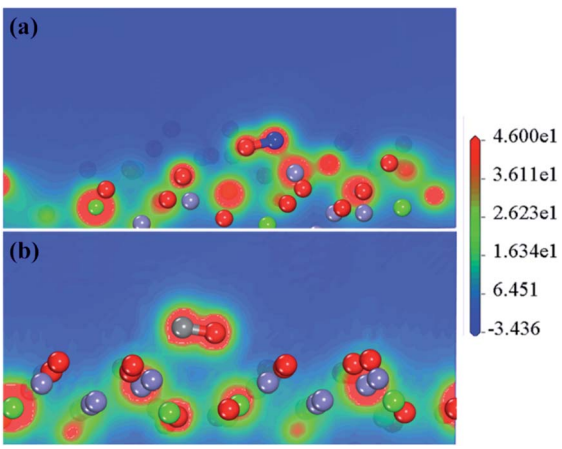

Fig. 6 Electron density of the catalytic reaction system after NO adsorption (a) and CO adsorption (b). (Grey, red, blue, green, and purple spheres represent carbon, oxygen, nitrogen, calcium, and iron atoms, respectively.)

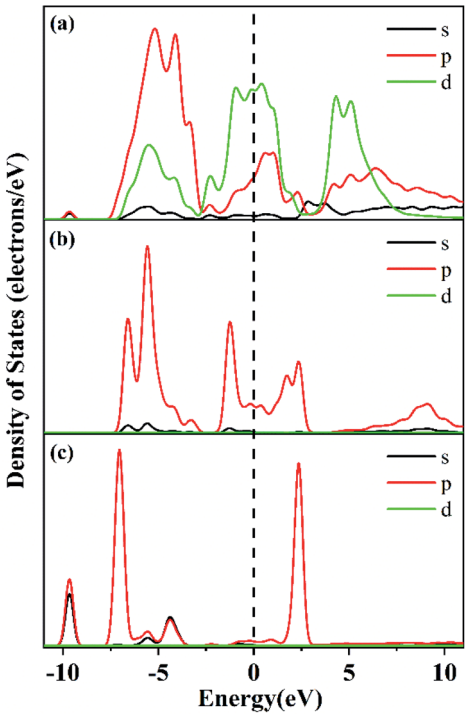

Fig. 7 The partial density of states of (a) $CaFe_2O_4$ + CO + NO, (b) NO adsorption on $CaFe_2O_4$, and (c) CO adsorption on $CaFe_2O_4$.

density of states (Fig. 7) also shows that NO-adsorbed electrons enter the catalyst's conduction band and valence band near the Fermi surface, causing the Fermi surface of the catalyst to move upwards. The CO adsorption does not affect the catalyst's conduction band near the Fermi surface. All the results indicate that the reaction proceeds by NO adsorption on the oxygen near the Fe atom, and that activation dissociation occurs first. The results are consistent with previous experimental results.

Combined with the previous results of adsorption energy, work function, density of states, and surface interaction analysis before and after adsorption, and the desorption rate-control step is CO_2 desorption. The elementary reaction path of this reaction can be set as follows:

Adsorption:

$$CO\ (g) + CaFe_2O_4\ (110) \leftrightarrow CO\ (a)$$

$$NO\ (g) + CaFe_2O_4\ (110) \leftrightarrow NO\ (a)$$

NO dissociation:

$$NO\ (a) \rightarrow N\cdot\ (a) + O\cdot\ (a)\ (RDS)$$

Reaction:

$$CO\ (a) + O\cdot\ (a) \rightarrow CO_2\ (a)$$

$$N\cdot\ (a) + N\cdot\ (a) \rightarrow N_2\ (a)$$

$$N\cdot\ (a) + NO\ (a) \rightarrow N_2O\ (a)$$

$$N\cdot\ (a) + CO\ (g) \rightarrow NCO\cdot\ (a)$$

$$NCO\cdot\ (a) + NO\ (g) \rightarrow CO_2\ (a) + N_2\ (a)$$

$$N_2O\ (a) \rightarrow N_2\ (a) + O\cdot\ (a)$$

Desorption:

$$N_2\ (a) \rightarrow N_2\ (g) + CaFe_2O_4\ (110)$$

$$CO_2\ (a) \rightarrow CO_2\ (g) + CaFe_2O_4\ (110)$$

Total reaction equation:

$$2CO\ (g) + 2NO\ (g) \rightarrow N_2\ (g) + 2CO_2\ (g)$$

where, the CO (g), NO (g), N_2 (g), and CO_2 (g) denote the gaseous CO, NO, N_2, and CO_2, the CO (a), NO (a), N_2 (a), and CO_2 (a) represent the adsorbed CO, NO, N_2, and CO_2 on the catalyst surface, and the N· (a), O· (a), and NCO· (a) represent the adsorbed nitrogen free radicals, oxygen free radicals, and NCO free radicals on the catalyst $CaFe_2O_4$ (110) surface, respectively.

The variations in the Gibbs free energy and activation energy for the reactions with different paths were obtained as shown in Fig. 8. The reaction rate-control step is NO (a) dissociation ($\Delta^{\neq}G$ = 9.047 eV). First, NO (a) are activated and dissociated near the Fe atoms of the $CaFe_2O_4$ (110) surface. Next, the dissociated oxygen free radical (O· (a)) reacts with the adsorbed CO (CO (a)) to form CO_2 (a) ($\Delta^{\neq}G = -8.096$ eV). The dissociated nitrogen free radicals (N· (a)) follow three paths (Fig. 9): ① one N· (a) combines with the NO (a) to generate the N_2O (a) intermediate ($\Delta^{\neq}G$ = 0.1206 eV). The N_2O (a) are unstable and decompose into N_2 (a) and O· (a) ($\Delta^{\neq}G = -4.132$ eV). ② Two N· (a) are combined to form N_2 (N_2 (a)) ($\Delta^{\neq}G = -20.368$ eV). ③ One N· (a)

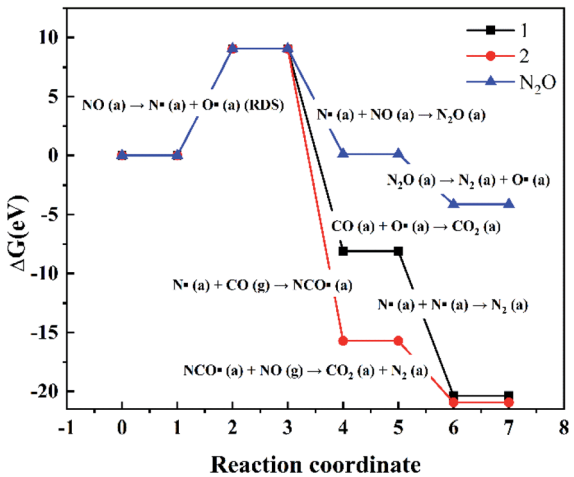

Fig. 8 The variation in the Gibbs free energy and activation energy for the reactions with different paths on the $CaFe_2O_4$ (110) at 298.15 K and 1 atm.

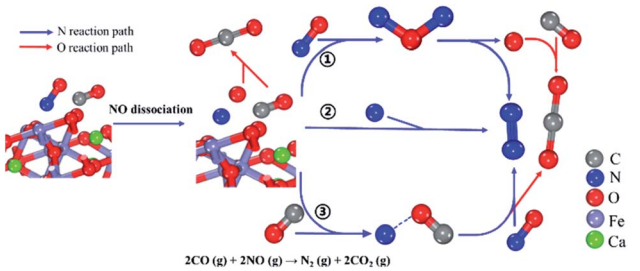

Fig. 9 Proposed mechanism of CO–NO reaction catalysed by $CaFe_2O_4$ in sintering.

combines with the CO (g) to generate the NCO· (a) intermediate ($\Delta^{\neq}G = -15.697$ eV), and then the NCO· (a) intermediate will continue to react with the NO (g) to form stable CO_2 (a) and N_2 (a) ($\Delta^{\neq}G = -5.235$ eV). These results are exactly the same as that of the previous experimental phenomena, in which N_2O gas is not observed.

In addition, we also can find that the CO has a weak physical adsorption interaction with the $CaFe_2O_4$ (110) surface from the results of the adsorption energy and the DOS in the calculation results. However, the CO adsorption interaction is very weak and the structure of the adsorbed CO is also very unstable, so it is almost impossible to be measured in the case of excessive CO (g) in the actual reaction, and the calculation results also show that CO is mainly in a gaseous state participated in the reaction from the results of the Gibbs free energy and activation energy. Therefore, the trace amounts of CO (a) only reaction with O· (a) to form CO_2 (a), and a large amount of CO (g) mainly reaction with N· (a) to generate the NCO· (a) intermediate.

Furthermore, since the collision probability of the two nitrogen free radicals is very small, and the Gibbs free energy variation in the NCO· intermediate is also very low, the reaction path of the NCO· intermediate is more likely to occur in the case of excessive CO (g) in the actual reaction, which is consistent with the previous experimental results.

3.4 Effect of reaction atmosphere

To further confirm this conclusion, $CaFe_2O_4$ was selected to conduct an additional reaction analysis. The rate of NO conversion was examined by changing the ratio of NO to CO in the reactor feed. Fig. 10 shows the effect of changing the CO concentration ratio on the conversion and the normalized conversion rate at a fixed NO feed concentration of 400 ppm. Fig. 11 shows the effect of changing NO concentration when the concentration of CO is fixed at 1%. Examining Fig. 10, it is found that increased concentration of CO in the reactant feed improves both, the conversion of NO as well as the rate of NO disappearance (Fig. 10 inset). The result is more significant given the fact that the enhanced rate of NO disappearance is even observed when CO concentration is 8000 ppm. This demonstrates that a CO molecule does not provide any competition to the NO molecule for site occupancy on the catalyst surface and that the CO participates in the reaction in a gaseous state. This observation is supported by the data

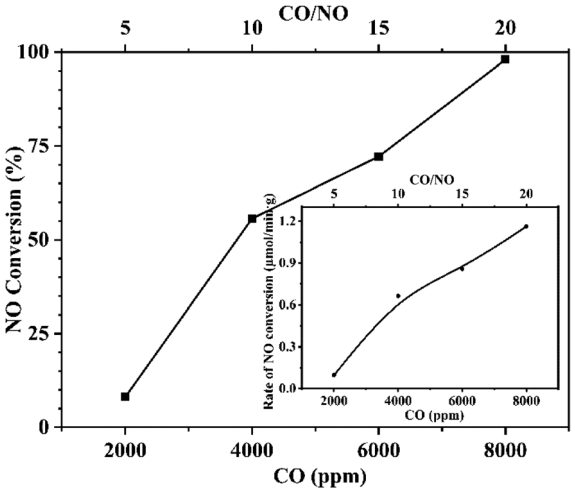

Fig. 10 Effect of CO concentration on NO conversion. Inset: effect of CO concentration on NO conversion rate. Reaction conditions: fixed NO concentration of 400 ppm, varied CO concentration from 2000 ppm to 8000 ppm, Ar balance, GHSV 95 000 h^{-1}.

shown in Fig. 11 and Fig. 11-inset, which show that an increase in NO concentration from 200 to 400 ppm while maintaining a fixed concentration of CO resulted in increasing the NO conversion while the rate of NO conversion peaks to a maximum. Further increase of NO concentration to 500 ppm leads to the decrease of reaction rate, and the conversion rate tends to be stable because the adsorbed NO cannot be dissociated in time. The above analysis further proves the fact that the CO participates in the reaction in the gaseous state, and the adsorption and dissociation of NO is the rapid step in the reaction. This phenomenon inspired us to propose a flue gas recirculation process to enhance NO_x emission reduction. A bellows with high CO concentration can be selected to increase the CO concentration in the circulating flue gas, thus promoting

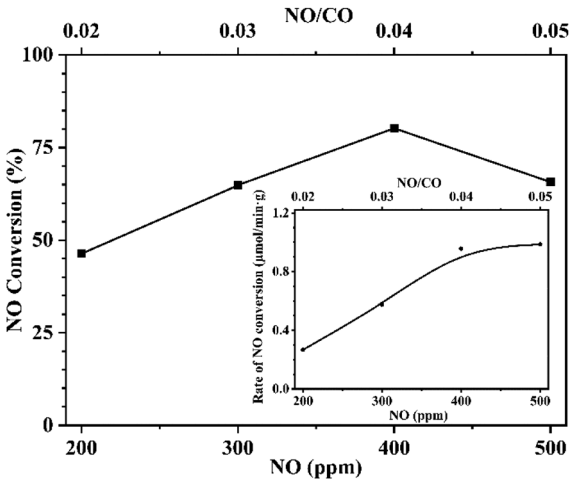

Fig. 11 Effect of NO concentration on NO conversion. Inset: effect of NO concentration on NO conversion rate. Reaction conditions: fixed CO concentration of 10 000 ppm, varied NO concentration from 200 ppm to 500 ppm, Ar balance, GHSV 95 000 h^{-1}.

the reduction of NO in the sintered bed and enhancing the NO_x reduction effect of flue gas recycling.

4. Conclusions

In the present work, we confirmed that $CaFe_2O_4$ shows a significant catalytic effect on the CO–NO reaction in the flue gas recirculation. On this basis, we carefully investigated the reaction mechanism and reaction path. Both the *in situ* DRIFTS experiments and DFT calculations all demonstrated that the CO–NO reaction on the surface of $CaFe_2O_4$ accorded with the Eley–Rideal mechanism. And the results show that the reaction is dominated by free radicals. Firstly, NO is adsorbed on the surface of $CaFe_2O_4$, and the adsorbed NO will be dissociated into nitrogen radicals and oxygen radicals to continue, which is also the rate-determining step of the reaction. Next, the dissociated nitrogen radicals will react with gaseous CO to form isocyanate radicals, the isocyanate radicals further react with gaseous NO to form CO_2 and N_2. Intensive experiment studies have also verified the limitations of free radicals and further confirmed that increasing the concentration of CO during flue gas recycling is beneficial to reduce this limitation, which provides new theoretical guidance for the design of the flue gas circulation process.

Conflicts of interest

There are no conflicts to declare.

Acknowledgements

This work was supported by the National Key Research and Development Program of China (No. 2017YFC0210304), Hebei Science and Technology Major Special Projects (No. 19074013Z) and National Natural Science Foundation of China (No. 51938014).

References

1 P. C. Wang, L. Yao, Y. J. Pu, L. Yang, X. Jiang and W. J. Jiang, *RSC Adv.*, 2019, **9**, 36658–36663.
2 F. Xiaohui, Y. Zhiyuan and G. Min, *Ironmak. Steelmak.*, 2016, **43**, 403–410.
3 L. Lu, T. C. Ooi and X. Li, *Iron Ore*, 2015, 551–579.
4 S. Singh, M. A. Nahil, X. Sun, C. F. Wu, J. H. Chen, B. X. Shen and P. T. Williams, *Fuel*, 2013, **105**, 585–594.
5 F. M. Wang, B. X. Shen, S. W. Zhu and Z. Wang, *Fuel*, 2019, **249**, 54–60.
6 W. J. Zhang, G. F. Liu, J. Jiang, Y. C. Tan, Q. Wang, C. H. Gong, D. K. Shen and C. F. Wu, *RSC Adv.*, 2019, **9**, 32110–32120.
7 J. Q. Xu, H. L. Wang, F. Guo, C. Zhang and J. Q. Xie, *RSC Adv.*, 2019, **9**, 824–838.
8 X. Fan, Z. Yu, M. Gan, X. Chen, Q. Chen, S. Liu and Y. Huang, *ISIJ Int.*, 2015, **55**, 2074–2081.
9 G. Wang, Z. Wen, G. F. Lou, R. F. Dou, X. W. Li, X. L. Liu and F. Y. Su, *Int. J. Heat Mass Tran.*, 2016, **97**, 964–974.
10 Y. Chen, Z. Guo and G. Feng, *Int. J. Min. Met. Mater.*, 2011, **18**, 390–396.
11 B. V. Reddy and S. N. Khanna, *Phys. Rev. Lett.*, 2004, **93**, 068301.
12 W. J. Ni, H. F. Li, Y. Y. Zhang and Z. S. Zou, *Energies*, 2019, **12**, DOI: 10.3390/en12020213.
13 X. Fan, G. Wong, M. Gan, X. Chen, Z. Yu and Z. Ji, *J. Clean. Prod.*, 2019, **235**, 1549–1558.
14 G. Wang, Z. Wen, G. F. Lou, R. F. Dou, X. W. Li, X. L. Liu and F. Y. Su, *Appl. Therm. Eng.*, 2016, **102**, 648–660.
15 H. Zhang, M. Rao, Z. Fan, Y. Zhang, G. Li and T. Jiang, *ISIJ Int.*, 2012, **52**, 2139–2144.
16 Z. Yu, X. Fan, M. Gan, X. Chen and W. Lv, *JOM*, 2017, **69**, 1570–1574.
17 H. Zhou, M. Zhou, Z. Liu, M. Cheng and J. Chen, *Fuel*, 2016, **179**, 322–331.
18 H. Zhou, P. Ma, M. X. Zhou, Z. Y. Lai and M. Cheng, *J. Energy Inst.*, 2019, **92**, 1476–1486.
19 S. Takeshi, S. Wu, K. Morioka, E. Kasai and Y. Omori, *Tetsu to Hagané*, 1994, **80**, 276–281.
20 R. Mezibricky and M. Frohlichova, *J. Min. Metall. B Metall.*, 2018, **54**, 9–20.
21 X. Tang and D. Wang, *Sintering Theory and Technology*, 1992, 107–125.
22 X. Fan, Z. Yu, M. Gan, X. Chen and Y. Huang, *Ironmak. Steelmak.*, 2016, **43**, 712–719.
23 K. Taira, *Fuel*, 2019, **236**, 244–250.
24 M. Gan, Z. Y. Ji, X. H. Fan, Y. J. Zhao, X. L. Chen and Y. Fan, *J. Clean. Prod.*, 2019, **232**, 1335–1347.
25 K. Morioka, S. Inaba, M. Shimizu, K. Ano and T. Sugiyama, *ISIJ Int.*, 2000, **40**, 280–285.
26 X. L. Chen, X. H. Fan, M. Gan, Y. S. Huang and Z. Y. Yu, *Ironmak. Steelmak.*, 2018, **45**, 434–440.
27 Z. Y. Yu, X. H. Fan, M. Gan, X. L. Chen and W. Lv, *JOM*, 2017, **69**, 1570–1574.
28 M. Gan, X. H. Fan, Z. Y. Yu, X. L. Chen, Z. Y. Ji, W. Lv, S. Liu and Y. S. Huang, *Ironmak. Steelmak.*, 2016, **43**, 442–449.
29 H. Zhou, P. N. Ma, M. Cheng, M. X. Zhou and Y. W. Li, *ISIJ Int.*, 2018, **58**, 1650–1658.
30 M. D. Segall, P. J. D. Lindan, M. J. Probert, C. J. Pickard, P. J. Hasnip, S. J. Clark and M. C. Payne, *J. Phys. Condens. Matter*, 2002, **14**, 2717–2744.
31 J. P. Perdew, J. A. Chevary, S. H. Vosko, K. A. Jackson, M. R. Pederson, D. J. Singh and C. Fiolhais, *Phys. Rev. B: Condens. Matter Mater. Phys.*, 1993, **48**, 4978.
32 A. Zecchina, D. Scarano, S. Bordiga, G. Ricchiardi, G. Spoto and F. Geobaldo, *Catal. Today*, 1996, **27**, 403–435.
33 K. I. Hadjiivanov, *Catal. Rev.*, 2000, **42**, 71–144.
34 P. L. Sun, X. X. Cheng, Y. H. Lai, Z. Q. Wang, C. Y. Ma and J. C. Chang, *RSC Adv.*, 2018, **8**, 36604–36615.
35 D. D. Miller and R. Siriwardane, *Appl. Energy*, 2018, **224**, 708–716.